New Journal of Physics
The open access journal at the forefront of physics

Deutsche Physikalische Gesellschaft DPG IOP Institute of Physics

PAPER • OPEN ACCESS

Step-edge assisted large scale FeSe monolayer growth on epitaxial Bi_2Se_3 thin films

To cite this article: J Fikáek *et al* 2020 *New J. Phys.* **22** 073050

New Journal of Physics
The open access journal at the forefront of physics

Deutsche Physikalische Gesellschaft DPG
IOP Institute of Physics

Published in partnership with: Deutsche Physikalische Gesellschaft and the Institute of Physics

CrossMark

OPEN ACCESS

RECEIVED
3 April 2020

REVISED
27 May 2020

ACCEPTED FOR PUBLICATION
10 June 2020

PUBLISHED
27 July 2020

PAPER

Step-edge assisted large scale FeSe monolayer growth on epitaxial Bi_2Se_3 thin films

J Fikáček[1], P Procházka[2], V Stetsovych[1], S Průša[2], M Vondráček[1], L Kormoš[2], T Skála[3], P Vlaic[4], O Caha[1,5], K Carva[6], J Čechal[2], G Springholz[7] and J Honolka[1,8]

[1] Institute of Physics, Academy of Sciences of the Czech Republic, Na Slovance 2, 18221 Prague 8, Czech Republic
[2] CEITEC - Central European Institute of Technology, Brno University of Technology, Purkyňova 123, 612 00 Brno, Czech Republic
[3] Department of Surface and Plasma Science, Faculty of Mathematics and Physics, Charles University, V Holešovičkách 2, 18000 Prague 8, Czech Republic
[4] Biophysics Department, University of Medicine and Pharmacy 'Iuliu Hatieganu', 400023 Cluj-Napoca, Romania
[5] Department of Condensed Matter Physics, Masaryk University, Kotlářská 2, 61137 Brno, Czech Republic
[6] Department of Condensed Matter Physics, Faculty of Mathematics and Physics, Charles University, Ke Karlovu 5, 12116 Prague 2, Czech Republic
[7] Institute of Semiconductor and Solid State Physics, Johannes Kepler University, Altenbergerstrasse 69, 4040 Linz, Austria
[8] Author to whom any correspondence should be addressed.

E-mail: honolka@fzu.cz

Keywords: Fe-chalcogenides, topological insulators, FeSe, interface superconductivity, unconventional superconductivity

Abstract

Enhanced superconductivity of FeSe in the 2D limit on oxide surfaces as well as the prediction of *topological superconductivity* at the interface to topological insulators makes the fabrication of Fe-chalcogenide monolayers a topic of current interest. So far superconductive properties of the latter are mostly studied by scanning tunneling spectroscopy, which can detect gaps in the local density of states as an indicator for Cooper pairing. Direct macroscopic transport properties, which can prove or falsify a true superconducting phase, are yet widely unexplored due to the difficulty to grow monolayer films with homogeneous material properties on a larger scale. Here we report on a promising route to fabricate micron-scale continuous carpets of monolayer thick FeSe on Bi_2Se_3 topological insulators. In contrast to previous procedures based on ultraflat bulk Bi_2Se_3 surfaces, we use molecular beam epitaxy grown Bi_2Se_3 films with high step-edge densities (terrace widths 10–100 nm). We observe that step edges promote the almost strainless growth of coalescing FeSe domains without compromising the underlying Bi_2Se_3 crystal structure.

1. Introduction

FeSe is one of the youngest representatives of Fe-based superconductors with a critical temperature $T_c = 8$ K in the bulk. Due to its simple two-element tetragonal PbO structure with a layer unit cell (UC) height $c = 5.52$ Å it is since then studied intensively in search of the physics behind unconventional superconductivity (SC).

In the last years, the interest in Fe-chalcogenides grew again after T_c of FeSe was found enhanced by a factor of 20 in the thin-film limit at interfaces to non-conductive oxides, also coined *interface superconductivity* [1]. First theoretical approaches address the influence of strain [2], electron doping [3], and band bending effects at the interface, in particular the competition between spin density waves and antiferromagnetism [4], closely related to the appearance of unconventional SC. For an overview on recent developments see e.g. reference [5].

Interfacing Fe-chalcogenides with the special material class of topological insulators (TIs) [6] yet promises further interesting physics such as the predicted effect of *topological superconductivity* [7]. In 2016, prototypical chalcogenide-based Bi_2Ch_3 (Ch = Se, Te) TI single crystals were used as substrates to grow FeCh islands by Fe atom deposition and subsequent annealing (FeSe/Bi_2Se_3 and FeTe/Bi_2Te_3) [8, 9]. Local scanning tunneling spectroscopy (STS) on respective FeSe islands on Bi_2Se_3 (FeSe is SC in the bulk) showed

no gap in the local density of states (DOS) in the accessible range of temperatures $T \geqslant 5$K [9], while surprisingly respective FeTe on Bi_2Te_3 (FeTe is normal conducting in the bulk) develops a gap in the DOS at 6.5 K [10]. It is important to stress that the detection of a gap by local STS generally is not sufficient to prove SC.

For an understanding of SC in the FeCh monolayer (ML) limit, macroscopic lateral transport properties would need to be studied, which requires continuous FeCh MLs with homogeneous material properties. These are hard to achieve. Above mentioned STS studies reported ambiguities in the local FeCh island thicknesses (1–5 UC) and discontinuous surface morphologies on a larger scale, which contain areas whose surface termination and stoichiometry are yet unknown. As a consequence, lateral transport studies with the aim to understand interface SC were reported for bulk-like FeCh/Bi_2Ch_3 heterostructures only [11].

Here we report on a modified approach based on molecular beam epitaxy (MBE) grown Bi_2Se_3 thin films, where step-edge assisted growth allows to fabricate well-defined μm-scale wide FeSe ML carpets at an intact TI interface. In low-energy electron microscopy (LEEM) we observe that FeSe carpets consist of three equally prominent 60° rotated FeSe domains with an average lateral size of 50 nm, well beyond the expected Cooper pair length scales of 1 nm for Fe-chalcogenides [12]. Combining standard scanning tunneling microscopy (STM) with non-local, but highly surface sensitive techniques like ultraviolet photoemission spectroscopy (UPS) and low-energy ion scattering (LEIS), we show that FeSe growth by Fe-deposition and annealing is facilitated on MBE–Bi_2Se_3 compared to cleaved bulk Bi_2Se_3 surfaces. FeSe starts to grow already at low temperatures below $T = 100$ °C with considerably less tetragonal distortion and leaving the surface fully Se-terminated. The improved growth conditions are attributed to fast diffusion of excess Se adatoms toward Bi_2Se_3 terrace step-edges, where—unlike on atomically flat bulk Bi_2Se_3–FeSe islands are preferentially formed. We prove that during this growth mode Bi remains a spectator element according to the following overall growth equation:

$$\mathrm{Fe} + [\mathrm{Bi_2Se_3}] + \mathrm{Se} \rightarrow \mathrm{FeSe} + [\mathrm{Bi_2Se_3}]^{*}. \tag{1}$$

The asterisk * indicates that during growth the Bi_2Se_3 terraces rearrange locally.

At optimized growth conditions, angle-resolved photoemission spectroscopy (ARPES) and x-ray absorption spectoscopy (XAS) confirm the intact band structure of FeSe monolayers, which fits well to presented *ab initio* density functional theory (DFT) predictions. The described approach using thin MBE-grown Bi_2Se_3 substrates of 100 nm scale thickness on insulating BaF_2 thus provides the chemically well-defined and continuous FeSe layer system, necessary to potentially detect interfacial SC properties by lateral transport with a minimum shunt conductivity through the underlying Bi_2Se_3 TI layer.

2. Results and discussion

2.1. Fabrication of continuous FeSe monolayers on micrometer scales: in-situ LEIS, LEEM, and XPS characterisation

A thorough understanding of FeSe layer growth ontop of Bi_2Se_3 requires a careful *in situ* characterisation using various analysis techniques applied on one and the same sample. LEEM, LEIS and x-ray photoemission spectroscopy (XPS) results presented in this section were measured at the large-scale materials characterisation cluster at *CEITEC* and are directly comparable at each stage of the FeSe growth.

2D surface growth is known to be governed by complex atomic diffusion and chemical reaction processes, which crucially depend on the atomic structure of the surface. Here, surface analysis by LEIS is the method of choice, since among the various scattering techniques it has the highest possible surface sensitivity and senses mainly the terminating atomic layer of a surface [13]. Depending on the surface atomic geometry and the effectivity of the charge exchange processes between the projectile and surface atoms, the 2nd atomic layer can also contribute to the surface peak intensity [14].

We start our analysis with the initial decapping step to remove a protective Se-cap ontop of Bi_2Se_3 under UHV conditions [see methods in section 4] to receive a clean, well-defined Bi_2Se_3 surface. Figure 1(a) shows LEIS results using helium ions during the gradual Se decapping process induced by heating as described in detail in the supplementary of reference [15]. The progress of decapping can be quantified by the ratio of integrated Bi and Se signal intensities $r_{\mathrm{Bi/Se}} = I_{\mathrm{Bi}}/I_{\mathrm{Se}}$ in the LEIS spectra, which increases with elevating temperature as shown in figure 1(b) versus time and respective temperatures. At $T = (200 \pm 50)$ °C the ratio converges to $r_{\mathrm{Bi/Se}} = 1.3$, which corresponds well to the reference measurement on *in situ* cleaved bulk Bi_2Se_3 single crystals, which we assume to be Se-terminated. We comment here that Bi–Bi double layer

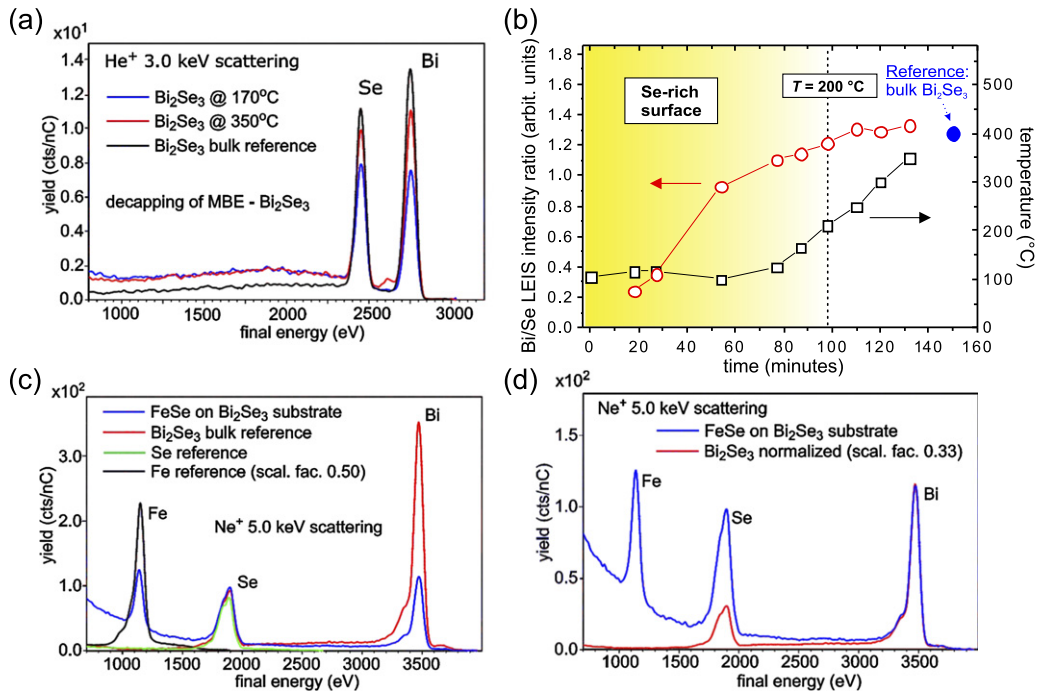

Figure 1. (a) LEIS data measured with He ions during removal of the Se cap. As a reference, data from a freshly cleaved bulk Bi_2Se_3 crystal surface is shown. (b) Temperature dependence of intensity ratios between Bi and Se LEIS signals during decapping. (c) and (d) show LEIS spectra with Ne ions before and after FeSe growth on decapped Bi_2Se_3. Reference spectra of pure Se and Fe have been added.

(DL) terminated Bi_2Se_3 was reported not to exhibit any Se LEIS intensity [16], and can thus be excluded in our case. This is consistent with our XPS data in figure 3(a) in the decapped state, where the Bi 5d core level (CL) peak structure shows a homogeneous shape typical for stoichiometric Bi_2Se_3. Metallic Bi components, e.g. due to Bi–Bi bonding, have not been detected. These should appear at a binding energy (EB) of 24.0 eV [17–19].

From respective XPS data of Se CLs in figure 3(b), we estimate extra Se coverages on the surface to be well below 1 ML, since a metallic Se component expected at 54.8 eV [20] (observed e.g. on an intact Se cap) is not detectable. Instead, a Se 3d spectrum typical for clean Bi_2Se_3 is visible. This can be fitted well by a spin–orbit split doublet Se^{I+II} plotted in (b), representing Se in Se-I and Se-II states in the Se(I)–Bi–Se(II)–Bi–Se(I) sequence of a Bi_2Se_3 quintuple layer (QL).

Figures 2(a) and (b) shows respective LEEM results of the bare Bi_2Se_3 in the decapped stage. LEEM gives local information on the crystal order on the surface with high spatial resolution. Switching between real space in figure 2(a) and the μ-diffraction mode of LEEM at 28 eV in figure 2(b) the well-known domain structure in MBE-grown Bi_2Se_3 [21] can be imaged in the dark field (DF) mode [see (a), right panel] with a spatial resolution of 5 nm. Scanning over the domains, the μ-diffraction pattern switches between the two 60°-rotated threefold symmetries of the Bi_2Se_3(0001) surface.

From our results we infer that decapped MBE-grown Bi_2Se_3 is (i) Se-terminated at decapping temperatures in the range $T = (300 \pm 50)$ °C and (ii) considerably Se-rich at decapping temperatures below $T = (200 \pm 50)$ °C as indicated in figure 1(b). We expect that Se-rich surface conditions are beneficial to grow high-quality FeSe layers, and help to avoid formation of Bi-containing phases other than that of Bi_2Se_3.

The FeSe growth is initiated by Fe deposition at room temperature (RT) with Fe coverages of about 1 ML. In LEEM the diffraction patterns immediately disappear due to the disorder introduced by randomly positioned Fe atoms on the surface. During subsequent annealing, the formation of ordered FeSe was monitored live in the μ-diffraction mode of LEEM. As shown in figures 2(c)–(d), the intensity of the 12-fold pattern is particularly visible at an energy of 18 eV, while at 28 eV the six-fold pattern of Bi_2Se_3 is dominant. Rectangular Brillouin zones (BZs) of the three FeSe domains [D_1, D_2 and D_3] are sketched in (d) and the energy dependence of respective diffraction intensities are compared to that of six-fold Bi_2Se_3 in (e). For Bi_2Se_3 spots (magenta) a pronounced and extended oscillatory behavior of the spot intensities is visible in the measured energy range 15–35 eV, evidencing high crystalline surface order. In contrast, respective intensities of FeSe spots (green) show a monotoneous decay without prominent oscillations. A similar decay is also observed for the specular (0, 0) spot (not shown here). Recent literature stresses the

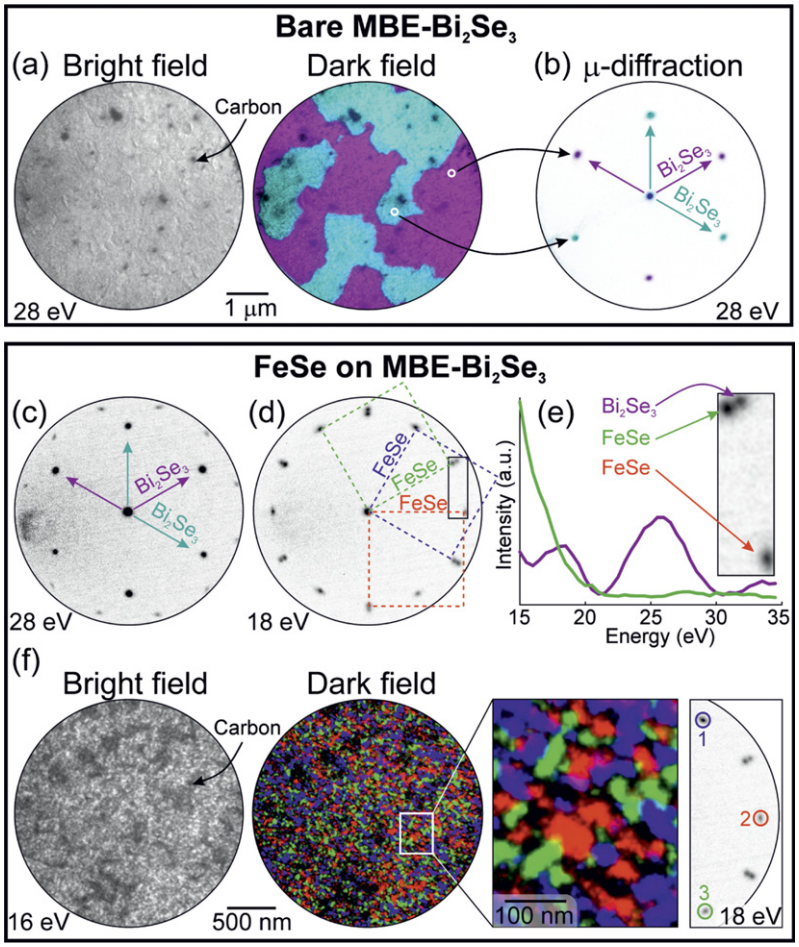

Figure 2. LEEM results in bright/dark-field real space microscopy and μ-diffraction modes for decapped Bi_2Se_3 [(a) and (b)] and FeSe on Bi_2Se_3 [(c)–(f)]. In (d) the orientation of three FeSe rotational domains [D_1, D_2, and D_3] are sketched in reciprocal space. (e) Plots of the energy dependent intensity of FeSe and Bi_2Se_3 diffraction spots shown in the inset.

large potential of energy-dependent LEEM reflectance data to extract thickness and electronic properties of substrate-supported few-layer 2D materials via phase accumulation models [22, 23]. Due to the limited energy range of our measured diffraction intensities in figure 2(e), such quantitative efforts are beyond the scope of this work. Qualitatively, our observation can nevertheless be taken as a first indication for ML growth of FeSe: a similar loss of oscillatory behavior in the low energy range and appearance of monotoneous intensity decay was observed for graphene at the transition from the multiple-layer regime to a single layer on Pt(111) [24], SiC [25], or SiO_2 [26] substrates. A monotoneous decay in the 2D graphene limit is predicted for a close proximity of a metallic substrate, depending also on the presence of interface states [23]. In our case interface states of FeSe could emerge from topological surface states and quantum-well states of the Bi_2Se_3 substrate [27].

Looking more closely into the diffraction data at 18 eV, lattice constants of FeSe and Bi_2Se_3 can be compared. The relative distance between the diffractive spots of FeSe and Bi_2Se_3 [shown enlarged in the inset of (e)] corresponds to 0.951 ± 0.003. Using the Bi_2Se_3 in-plane lattice parameter of $a_{Bi2Se3} = 4.139$ Å as a reference, we obtain a FeSe lattice parameter of $a_{FeSe} = 3.769 \pm 0.012$ Å. Within the experimental error this value corresponds to the bulk FeSe lattice parameter of 3.773 Å. Evaluating the second lateral FeSe lattice constant b_{FeSe} in the respective 90° rotated diffraction spots, we find a small average contraction by $(0.5 \pm 0.3)\%$ compared to a_{FeSe}. With respect to bulk Bi_2Se_3 substrates (2% tetragonal distortion) [8] FeSe thus grows significantly relaxed on MBE–Bi_2Se_3, with in-plane lattice constants comparable to those of the SC bulk FeSe phase. From the absence of other diffraction spots we moreover conclude that areal coverages of phases other than Bi_2Se_3 or FeSe are negligible.

LEIS data using Neon ions for the very same FeSe/Bi_2Se_3 sample state of figures 2(c)–(f) are summarized in figure 1(c). LEIS exhibits an additional Fe peak and a reduced Bi intensity with respect to decapped Bi_2Se_3 as expected for a FeSe layer covering the Bi_2Se_3 substrate. A comparison of LEIS spectra on FeSe/Bi_2Se_3 with reference samples of cleaved bulk Bi_2Se_3 and pure Se show equivalent Se peak intensities, evidencing fully Se-terminated surfaces in all three cases within the resolution of the experiment.

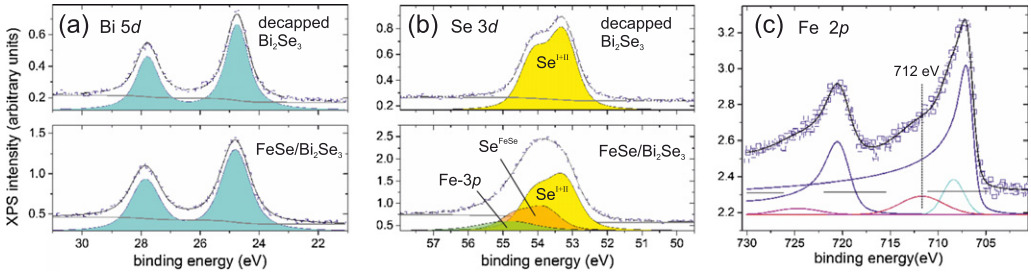

Figure 3. XPS measurements ($h\nu = 1.254$ keV) on bare Bi_2Se_3 decapped at $T = (200 \pm 50)$ °C (pass energy $E_p = 15$ eV) and after Fe deposition and annealing at $T = (200 \pm 50)$ °C ($E_p = 30$ eV). (a) and (b) show Bi 5d and Se 3d CLs, respectively. Se 3d fits were generated as explained in the main text. (c) Shows the Fe 2p CL after FeSe growth together with fits based on asymmetric Doniach–Šunjić profiles and minor Voigt components (see methods section 4 for further details).

LEIS spectrum of Bi_2Se_3 has to be multiplied by a factor of 0.33 as to have a Bi peak intensity the same like that of FeSe/Bi_2Se_3 [see figure 1(d)]. The shape of the Bi peak is identical within the experimental resolution. From surface areas terminated by Se–Fe–Se trilayers we expect no Bi signal in LEIS, since LEIS is probing only 1–2 atomic layers. Thus, 33% of the surface area gives a Bi signal corresponding to that of Bi_2Se_3.

To further clarify the origin of the Bi signals visible in LEIS, we show respective XPS spectra in figures 3(a) and (b), which give important information about the Bi and Se bonding states. Upon FeSe growth, we observe strong changes mainly in the Se 3d CL shape, when compared to Bi_2Se_3. This is expected, because Se atoms are differently coordinated in FeSe, which will lead to a characteristic chemical shift in XPS compared to Bi_2Se_3. Indeed, in figure 3(b) we fit the Se 3d CL spectrum well by adding one single Se^{FeSe} component to the Bi_2Se_3-specific Se^{I+II} doublet. Hereby, we take into account a minor Fe 3p intensity, which is expected to appear at EB = 55 eV [28]. The main Fe $2p_{3/2}$ peak position shown in figure 3(c) is at 707 eV, which corresponds to that of metallic Fe. The metal character of Fe in FeSe is corroborated by the dominating metallic asymmetric Doniach–Šunjić component in the fit of the Fe $2p_{3/2}$ CL added in figure 3(c). However, our fit reveals also a broad satellite intensity at 712 eV, evidencing partly covalent character of Fe 3d states due to hybridsation with Te orbitals as we discuss further in section 2.2.

In contrast to Se, Bi 5d CLs in figure 3(a) appear unchanged upon FeSe growth, which—as we further prove in section 2.3 with higher surface sensitivity—is due to an intact chemical Bi_2Se_3 QL structure at the surface and a passive role of Bi in the overall reaction described in equation (1). The absence of a shoulder at EB = 24.0 eV once more confirms that also after FeSe growth, metallic Bi–Bi bonding (e.g. from Bi-clusters or extended Bi–Bi DLs [18] expected in Bi_4Se_3 or Bi_1Se_1 phases) or metallic Bi–Fe bonding are negligible within the XPS probing depth of about 20 Å [15]. For a rough estimation of the FeSe thickness, we can compare the intensity ratio of the two Se 3d components Se^{FeSe} and Se^{I+II} in figure 3(b). Following Seah *et al* [29], we estimate the average FeSe thickness to be (7.5 ± 1.0) Å, which corresponds to 1.3 UCs.

The areal distribution of FeSe and Bi_2Se_3 surface terminations can be directly imaged by DF LEEM, summarized in figure 2(f). For DF imaging, refractive spots of the three FeSe domains [see (f), right panel] were chosen. The DF image reveals a carpet of three FeSe domain orientations with approximately equal areal coverage, which extends over the whole sample surface. Typical domain sizes are 50 nm. Their shapes appear elongated along the high-symmetry directions and step-edges of the underlying Bi_2Se_3, an effect which will be discussed in detail on the basis of STM data in section 2.3. From the spatial resolution 5 nm in the DF mode, we estimate a total areal FeSe coverage of (72 ± 5)% in excellent agreement with the LEIS estimation of (67 ± 3)% .

2.2. Electronic band structure characterisation of FeSe monolayer growth on MBE–Bi_2Se_3

Again we start our discussion in the decapped state prior to FeSe growth. Figure 4(a) displays the measured ARPES intensity of decapped Bi_2Se_3 at EB = 0.8 eV, corresponding to an energy cut just below the valence band maximum (VBM) located at EB = 0.7 eV. The position of the VBM was estimated from the respective *k*-space integrated UPS data shown in figure 4(g), by fitting a tangential line shown in red. The *k*-space range in (a) covers the full trigonal 1st BZ around $\bar{\Gamma}$ (marked in white) and extends beyond the six $\bar{\Gamma}$ points from the 2nd BZs (denoted $\bar{\Gamma}'$). A six-fold symmetry of ARPES patterns is expected from the UV light spot size of several hundreds of micrometers, which averages over many equally prominent 60° Bi_2Se_3 domains observed by DF LEEM described in section 2.1. (k, E)-cuts along the high symmetry directions $\bar{M} - \bar{\Gamma} - \bar{M}$

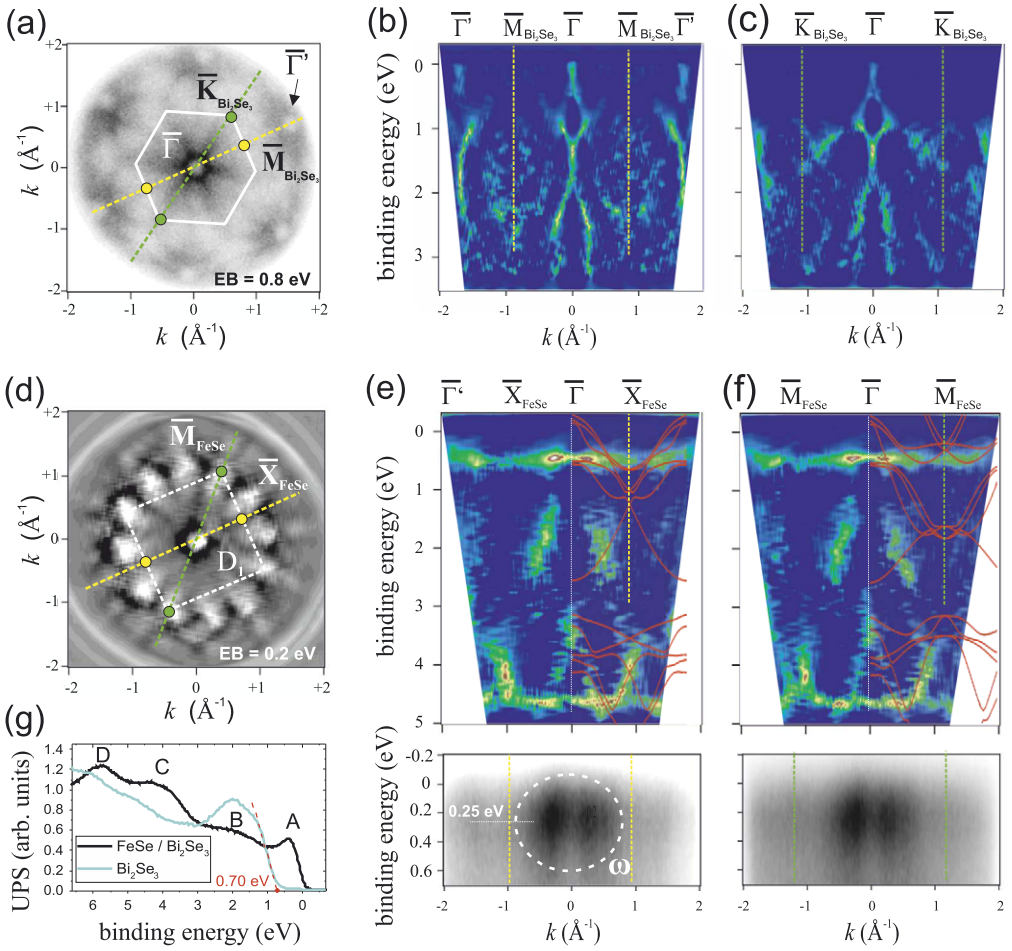

Figure 4. k-PEEM data at $h\nu = 21.2$ eV of (a)–(c) bare Bi_2Se_3 decapped at $T = 180$ °C and (d)–(f) FeSe/Bi_2Se_3 after FeSe growth at $T = 250$ °C. All data is plotted in 2nd derivative contrast. Lower panels of (e) and (f) show original data close to E_F in more detail. (g) Plots of the k-space integrated UPS intensities of Bi_2Se_3 and FeSe/Bi_2Se_3.

and $\bar{K} - \bar{\Gamma} - \bar{K}$ are shown with 2nd derivative contrast in (b) and (c), respectively. At $\bar{\Gamma}$ and $\bar{\Gamma}'$, n-doped topological surface states (TSSs) are visible with Dirac points located 0.2 eV below the Fermi level (E_F). In the UPS signal shown in figure 4(g) TSSs appear as a weak plateau-like intensity above the Bi_2Se_3 VBM at 0.7 eV.

Figures 4(d)–(f) summarizes respective photoemission data after FeSe growth (Fe deposition of approximately 1 ML coverage at RT and subsequent annealing at $T = 250$°C for 30 min). Fe 3d, Bi 5d and Se 3d CL intensities were measured *in situ* by XPS and compared to figure 3, to verify a comparable FeSe coverage as the samples characterized in section 2.1. A (k_x, k_y)-cut at EB = 0.2 eV shows the characteristic 12-fold symmetric k-space pattern of the three equally prominent FeSe domains [figure 4(d)], which is equivalent to the LEEM pattern in figure 2(d) of section 2.1. The BZ of one domain (D_1) is marked as a square with according high symmetry directions $\bar{X}_{FeSe}$ and $\bar{M}_{FeSe}$. Respective (k, E) cuts along $\bar{X}_{FeSe} - \bar{\Gamma} - \bar{X}_{FeSe}$ and $\bar{M}_{FeSe} - \bar{\Gamma} - \bar{M}_{FeSe}$ are shown in figures 4(e) and (f). First we notice that after FeSe growth—in contrast to related reports in the literature [9]—we do not observe traces of the Bi_2Se_3 band structure, which is in line with the quasi-continuous FeSe layer coverage in our case [see section 2.1]. Secondly, we notice that the cuts in figures 4(e) and (f) are very similar within the limited resolution of our experiment. This is not surprising, since in figure 4(e) the $\bar{\Gamma} - \bar{X}_{FeSe}$ signal from domain D_1 is mixed with two signals from domains D_2 and D_3 [not drawn in (d)], which correspond to cuts $\pm 15°$ rotated from $\bar{\Gamma} - \bar{M}_{FeSe}$. Similarly, in figure 4(f) the $\bar{\Gamma} - \bar{M}_{FeSe}$ signal is mixed with cuts $\pm 15°$ rotated $\bar{\Gamma} - \bar{X}_{FeSe}$. For comparison, we added DFT calculated band structure cuts $\Gamma - M_{FeSe}$ and $\Gamma - X_{FeSe}$ expected for bulk FeSe [full DFT results are plotted as black lines in figure 5(a)]. Details on the DFT methods are described in section 4. A good coincidence of the experiment with theory on bulk FeSe is observed, particularly in the range EB = 3.0–5.0 eV where strongly dispersing Fe 3d–Se 4p hybridised bands dominate the band structure. Following the argumentation of Arnold *et al* [30] we comment here that the strong differences in

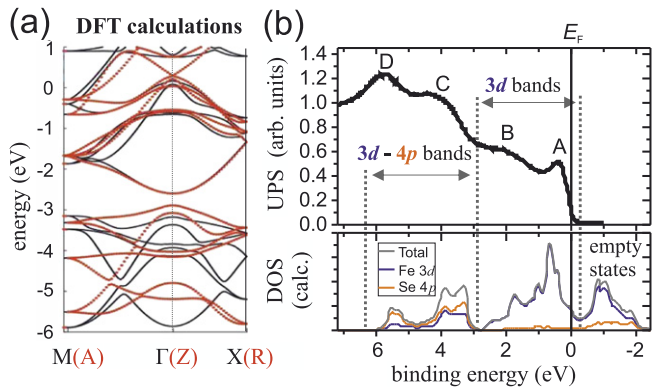

Figure 5. (a) DFT calculations of the bulk FeSe band structure. Black lines correspond to cuts at $k_z = 0$ (cut through Γ-M-X) and red lines to cuts at the BZ border (cut through Z-A-R), according to the BZ definition of reference [30]. (b) Upper panel: k-space integrated experimental UPS data of FeSe/Bi_2Se_3. Lower panel: calculated DOS and respective projections on Fe 3d and Se 4p states.

the calculated band structure for Γ-*M*-*X* and Z-*A*-*R* directions in this energy range [black and red lines in figure 5(a)] reflect the 3D character of these bands.

In the energy range EB = 1.5–2.5 eV of figures 4(e) and (f), measured bands appear to be particularly broad and not well represented by our DFT calculations. Our ground state calculations do not contain any renormalization procedures, and the observed broadening might be captured e.g. by theory approaches including incoherent many-body excitations in Fe 3d states [31].

Closer to E_F a camel-back shaped band appears at EB = 0.25 eV near $\bar{\Gamma}$, which we show in detail in the lower panels of figures 4(e) and (f). This band is often denoted as ω band and has been observed in FeSe/STO interfaces [32] but also in the Te-based counterpart FeTe/Bi_2Te_3 [30] at comparable EBs. It is characteristic for the FeCh band structure [see e.g. theory in references [33, 34]].

Due to the domain-averaging of ARPES signals in any chosen $k_{\|}$ direction it is instructive to look at the UPS signal, which should be equivalent for all rotational domains D_1–D_3. In contrast to decapped Bi_2Se_3, the UPS shown in figure 4(g) has a large, metallic spectral weight at E_F and exhibits four prominent peaks labeled as A, B, C and D in the EB range up to 6 eV. When comparing the UPS data after FeSe growth with our respective DFT calculated DOS in figure 5(b), we can assign peaks A and B to the Fe 3d-dominated band structure, while C and D are strongly hybridised states composed of Se 4p and Fe 3d states. The energy position of the sharp peak A appears closer to E_F in the experiment compared to theory. Indeed, DMFT methods were reported to be more suitable to reproduce low-energy band structure as they seem capture local Coulomb interactions and Hund's coupling effects [31].

In contrast to the occupied band structure with almost pure Fe 3d orbital character, the calculated unoccupied counterpart in figure 5(b) suggests considerable mixing of Fe 3d and Se 4p states in the energy range [−0.5, −2] eV above E_F. Unoccupied states are not accessible by standard photoemisson, but can be probed by XAS at the Fe $L_{3,2}$ edges, which correspond to dipole transitions $2p^6 3d^n \rightarrow 2p^5 3d^{n+1}$ from localized spin–orbit split 2p CLs ($2p_{1/2}$ and $2p_{3/2}$) into empty 3d states. We stress that XAS data provides information on empty Fe states in the presence of a 2p core hole, and thus does not directly reflect the empty DOS in its ground state.

In figure 6 we show temperature dependent XAS spectra of FeSe/Bi_2Se_3 at the Fe $L_{3,2}$ edges using left (+) and right (−) circularly polarized light in polar geometry ($\Theta = 0°$ as depicted in the inset). Respective temperature dependent x-ray magnetic circular dichroism (XMCD) spectra in small fields of 0.2 T do not show any magnetic response as expected for non-ferromagnetic systems. The average non-dichroic XAS spectra XAS = ($XAS^+ + XAS^-$) exhibit no sharp multiplet structures and the L_3 peak is located at 708.0 eV, similar to bulk Fe (707.5 eV). Core–hole interactions in the $2p^5 3d^{n+1}$ state are thus considerably screened by free carriers. However, compared to metallic Fe, L_3 and L_2 resonances are narrower and with a shoulder at about 712.0 eV, which appears 3.8 eV above the L_3 peak as indicated by an arrow in figure 6. It should be noted that a similar shoulder separated by 4.5 eV was observed also by direct probing of the unoccupied DOS of bulk FeSe by light inverse photoemission spectroscopy in the UV range [35]. For bulk Fe-chalcogenides like FeSe [36] or $CsFe_2Se_3$ [37], this shoulder in the XAS signal can be understood within a tetrahedral $FeCh_4$ cluster model taking into account 3d–3d Coulomb energy ($U = 1.5$ eV) and charge transfer between chalcogen 4p-ligands and 3d orbitals (Slater–Koster parameters $pd\sigma = -1.5$ and $pd\pi = +0.69$ eV for hybridization terms between d^6 and $d^7\underline{L}$ configurations) [36]. The shoulder thus is in

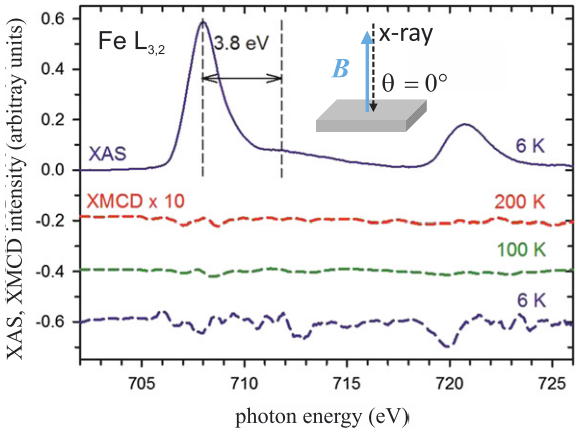

Figure 6. XAS and respective XMCD spectra of FeSe on Bi_2Se_3 taken at temperatures $T = 200, 100$, and 6 K. The inset shows the polar measuring geometry ($\Theta = 0°$) and the field orientation. XMCD signals were measured at $B = 0.2$ T and are shown enlarged by a factor of 10.

line with the considerable mixing of Fe 3d with Se 4p states in the unoccupied part of the DOS 1–2 eV above E_F suggested also by our calculations in figure 5(b).

From the L_3 and L_2 white line intensities in figure 6 we can further extract a large branching ratio I_{L3}/I_{L3+L2} of (0.72 ± 0.01) [I_{L3}/I_{L2} of (2.57 ± 0.03)], typical for a Hund's rule high-spin state of iron [38, 39]. To quantify the intensities I_{L3} and I_{L2}, we used standard evaluation procedures including the subtraction of a two-step function background as described e.g. in reference [40]. For non-metallic Fe-oxides, branching ratios of 0.73 and 0.75 were associated with d^6 (Fe^{2+}) and d^5 (Fe^{3+}) states [41]. In our case, the estimated position of the Fermi level in the calculated Fe 3d DOS shown in figure 5(b) suggests a d-shell occupancy of 6.2, supporting the above discussed $FeCh_4$ cluster model cluster model based on a Fe d^6 configuration.

2.3. Step-edge assisted FeSe island growth dynamics

We finally want to understand our observation of a facilitated FeSe growth on MBE–Bi_2Se_3 substrates by looking into the growth dynamics on the atomic scale. From the similarity of Bi CL spectra before and after FeSe growth on Bi_2Se_3 (see figure 3), we concluded that Bi—in total—plays the role of a spectator element in the FeSe growth process. This finding is surprising at first glance since Fe atoms deposited on Bi_2Se_3 and Bi_2Te_3 surfaces both at room temperature or low temperatures are known to induce characteristic shoulders at EBs of about 24 eV in the Bi 5d edges [19, 28], evidencing considerable interaction between Fe and Bi. In the following, we will show that such shoulders are indeed visible in a transient state during the FeSe growth process, but disappear when FeSe fully develops. To that end, CLs had to be measured with higher resolution and higher surface sensitivity using synchrotron radiation at Elettra.

In figures 7(a) and (b), Bi 5d and Se 3d CLs are shown after 1 ML Fe deposition at room temperature and during subsequent annealing up to temperatures $T = (320 \pm 50)$ °C. CLs were measured at photon energies $h\nu = 130$ eV with a probing depth of only about 5 Å. After Fe deposition at RT the Bi 5d CL shape confirms the expected characteristic shoulder at 24 eV corresponding to a metallic-like Bi state induced by the presence of Fe, which is a consequence of the known heavy relaxation of 3d adatoms into the Bi_2Se_3 surface [19]. Due to the high surface sensitivity, only half of the Bi spectral intensity remains at an EB corresponding to that of the Bi_2Se_3 host state. Surprisingly, with the formation of FeSe during annealing the metallic state of Bi disappears entirely, while Fe 2p CLs intensities remain comparable [see figure 7(c)]. Fitting the Bi 5d spectra by two Bi components, the transfer of spectral weight from the metallic state to that of Bi_2Se_3 can be quantified. According temperature dependent spectral weights are plotted in figure 7(d). The original Bi chemical state corresponding to Bi_2Se_3 is thus fully restored when the FeSe growth is completed at about $T = (290 \pm 50)$ °C, which implies an intact QL structure in the final state as we suggest in equation (1). This is in line with our more bulk sensitive XPS measurements in figure 3 with a probing depth of about 20 Å.

Respective Se 3d spectra in figure 7(b) confirm our XPS results from section 2.1 but show Se^{I+II} and Se^{FeSe} components with much higher resolution. Surprisingly, components corresponding to Se^{FeSe} are present already at RT. The Se^{FeSe} spectral weight is stable up to $T = 290$ °C and decreases sigificantly at higher temperatures.

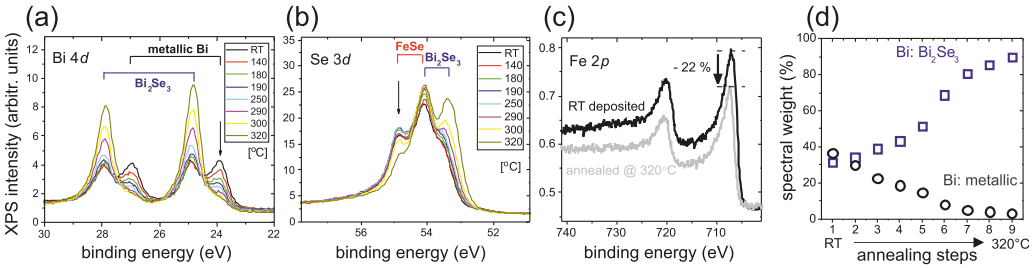

Figure 7. Monitoring FeSe formation in UPS at maximum surface sensitivity. Measurements are done at photon energies $h\nu = 130$ eV during an annealing cycle up to $T = (320 \pm 50)$ °C. (a) and (b) show Bi 5d and Se 3d CL spectra during progressive annealing. For comparison the Fe 2p XPS intensity measured at $h\nu = 900$ eV before and after annealing at the maximum temperature $T = (320 \pm 50)$ °C is shown in (c). (d) Development of the temperature dependent UPS spectral weight of Bi_2Se_3 and metallic Bi components in the Bi 5d spectra.

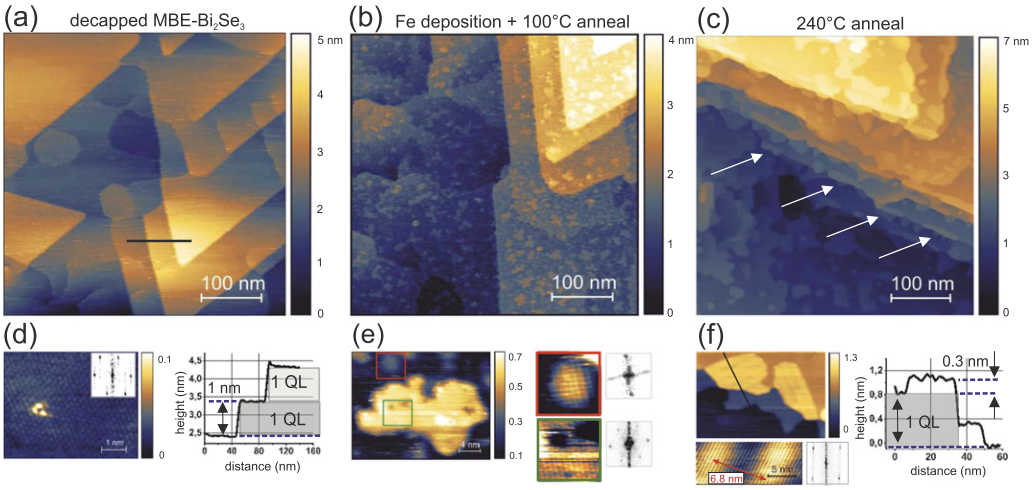

Figure 8. The upper row shows (400 nm × 400 nm) overview STM images at different stages of FeSe growth: (a) decapped Bi_2Se_3, (b) after 0.7 ML Fe deposition and annealing at (100 ± 30) °C, and (c) after annealing at (240 ± 50) °C. Examples of step-assisted FeSe growth areas are indicated by white arrows for one terrace. The bottom row (d)–(f) shows respective analysis on the nanometer scale with lines profiles. Images with atomic resolution are shown together with respective FFT images to the right. In (f) a Moiré pattern with periodicity (6.8 ± 0.3) nm is displayed.

In order to verify the formation of FeSe seeds at such low temperatures, we performed STM measurements at various stages of FeSe growth, summarized in figure 8. Figure 8(a) shows the typical morphology of a decapped bare MBE-grown Bi_2Se_3 surface, consisting of triangular shaped pyramids and a high density of QL steps of 1 nm height [see line profile in figure 8(d)].

After Fe deposition at RT, no atomic resolution could be achieved by STM, which we attribute to surface disorder in the presence of randomly positioned Fe and the reported partial diffusion into the first QL [42]. After annealing at $T = 100$ °C, however, small FeSe seeds of approximately 5 nm lateral size indeed become visible [see figures 8(b) and (e)]. The seeds show a characteristic 3.7 Å cubic atomic lattice with a typical height of (1.6 ± 0.2) Å with respect to the supporting Bi_2Se_3 terraces.

The surface structure after further annealing at $T = (240 \pm 50)$ °C has changed in several ways. Large FeSe islands have formed [see figures 8(c) and (f)] (typical island size of 50 nm similar to those observed in DF LEEM in figure 2), which exhibit the characteristic Moiré pattern with periodicity (6.8 ± 0.3) nm first reported by Cavallin *et al* in 2016 [8] on bulk Bi_2Se_3. In our case of MBE-grown Bi_2Se_3 surfaces, FeSe grows preferentially along the QL step-edges in an elongated fashion both on the higher and lower part of the QL steps as indicted in figure 8(c) by white arrows. A typical line scan is plotted in figure 8(f). With a height of (3.0 ± 0.2) Å with respect to Bi_2Se_3 terraces, these islands appear much higher than the low-temperature FeSe seeds. The Moiré height variation ±0.25 Å shown in figure 8(f) coincides well with previoulsy reported ones of FeSe on bulk Bi_2Se_3 [8, 9].

In the following, we discuss possible origins of the observed preferential formation of FeSe along Bi_2Se_3 step-edges. Island growth kinetics on surfaces is known to be determined by parameters of atom interlayer and terrace diffusion, as well as nucleation probabilities. Atomic diffusion processes at and across Bi_2Se_3 QL step-edges are especially complex, as the QL-high steps are composed of Se–Bi–Se–Bi–Se stacks and thus

cannot be modeled as a simple 1D diffusion barrier. Recent calculations propose that the efficient layer-by-layer growth of Bi_2Se_3 during MBE may be due to a step-edge heteroatomic barrier reduction mechanism, which e.g. reduces diffusion barriers for Se adatoms across QL barriers [43]. As a possible scenario for the step-assisted FeSe growth, we propose that randomly RT deposited Fe atoms start to migrate at elevated temperatures and get preferentially pinned at QL steps not only at the bottom (by high step-edge detachment barriers), but also the top (limited by a high Schwöbel barrier). Schwöbel barriers can be considered high, since in STM the FeSe coverage seems to scale with the terrace area signifying suppressed Fe diffusion across step edges. Observed Se-rich surface conditions of MBE–Bi_2Se_3 discussed in section 2.1 and respective fast Se adatom surface diffusion provide the necessary local excess Se concentration at the step-edges for FeSe seeds to form, while keeping the supporting Bi_2Se_3 terrace mostly intact.

3. Conclusions

We present a comprehensive study of a modified approach to grow FeSe layers on Bi_2Se_3 topological insulators on larger scales, starting from MBE-grown Bi_2Se_3 substrates. FeSe growth is initiated by Fe deposition (about 1 monolayer coverage) and subsequent annealing at elevated temperatures between 100 °C and 320 °C. The principle of growth was first reported by Cavallin *et al* [8] in 2016 on cleaved bulk Bi_2Se_3 surfaces, however FeSe coverage and the surface homogeneity after the growth has been under debate especially regarding the possible occurrence of FeSe multilayers and Bi-rich phases.

Using various surface sensitive techniques like low-energy ion scattering, low-energy electron microscopy, photoemission and x-ray absorption spectroscopy, we show that MBE-grown Bi_2Se_3 thin film substrates with a high density of step-edges are perfect seeding grounds for micrometer-scale FeSe monolayer growth with high coverage, high chemical order, and reduced compressive strain. Photoemission data on electronic properties agree well with predictions from our density functional theory calculations on FeSe composed of Fe atoms in a high-spin d^6 state.

From our scanning tunneling microscopy studies we attribute the facilitated growth on MBE-grown Bi_2Se_3 to preferential nucleation of Fe atoms along the many step-edges, which are rare in respective cleaved and atomically flat bulk Bi_2Se_3 substrates. Larger Se excess adatom concentrations on MBE-grown Bi_2Se_3 surfaces seem necessary for the formation of well-odered FeSe islands ontop of Bi_2Se_3 without compromising the underlying Bi_2Se_3 terrace stoichiometry.

The resulting FeSe domains of in average 50 nm lateral size significantly exceed expected Cooper pair length scales of 1 nm and form a coalescing carpet ontop of Bi_2Se_3. This renders this FeSe 2D material system a promising candidate to finally enable studies of unconventional superconductivity by macroscopic lateral transport experiments at the interface to a topological insulator.

4. Methods

Bi_2Se_3(0001) films were epitaxially grown on insulating BaF_2(111). The structural order of the material was monitored by reflection high energy electron diffraction as described in earlier works [15]. The epitaxial heterostructures were finally protected against oxidation by amorphous metallic Se cap layers, which allows to recover clean surfaces by an *in-situ* decapping procedure under ultra-high vacuum (UHV) conditions. FeSe growth on decapped Bi_2Se_3(0001) surfaces was done using a two-step procedure: (i) deposition of Fe coverages in the range 0.3–1.0 monolayers at room temperature and (ii) subsequent annealing at elevated temperatures. Fe evaporator fluxes were calibrated using a quartz balance and by comparison of Fe and (Bi, Se) XPS intensities, which were cross-referenced to coverages estimated from our STM data.

At the *CEITEC* nano core facility, one and the same sample can be *in situ* characterised by various surface sensitive techniques including low-energy electron microscopy (LEEM), low-energy ion scattering (LEIS) and x-ray photoelectron spectroscopy (XPS). LEEM/μ-LEED, LEIS and XPS measurements were performed in a complex UHV system with an FE-LEEM P90 (Specs GmbH), Qtac 100 (ION-TOF GmbH) and Phoibos 150 spectrometer, respectively. There, the samples were prepared in a separate UHV chamber and moved to the instruments for analysis via a linear transfer system under UHV conditions; the base pressure in all chambers was below 2×10^{-10} mbar. Bright field LEEM was done with electrons in the energy range [0, 35] eV from the (0, 0) diffracted beam. The diffraction and μ-diffraction patterns were collected from spots with elliptical shape of 15×10 μm^2 and circular area with a diameter of 185 nm. For LEIS measurements, the normal incidence primary beam of helium or neon ions with

characteristic diameter 50 μm was scanned over surface areas of about 2×2 mm^2. A double-thoroidal energy analyzer with full azimuthal acceptance maximizes the sensitivity of the instrument. This enables to minimize the surface modification during the measurement (static measurement conditions). Typical ion fluences for a single spectrum was 1.2×10^{14} He$^+$ ions/cm^2 and 0.3×10^{14} Ne$^+$ ions cm^2. The scattering angle was fixed at 145°. XPS experiments at *CEITEC* were performed by non-monochromatized Mg K$_\alpha$ radiation in normal emission geometry (emission angle 0°) at pass energies E_p of 15 eV and 30 eV.

k-PEEM measurements with laboratory light sources were done using an *Omicron NanoESCA* instrument located at the SAFMAT center in Prague. The photoemission spectrometer is based on a PEEM column and an imaging double hemispherical energy filter. A transfer lens in the electron optics switches between real space and *k*-PEEM mode, which also allows to do classical XPS with monochromatized Al K$_\alpha$ radiation. Energy dependent *k*-space mapping of the Brillouin zone (BZ) was performed using a helium discharge lamp at $h\nu = 21.2$ eV with an analyser kinetic energy resolution $\Delta E = 0.2$ eV. An overview on the used techniques can be found in reference [44]. For metallic samples, the Fermi edge E_F is derived from the kinetic energy at which the *k*-PEEM intensity disappears. We define this energy as zero binding energy and expect the error of this Fermi level estimation to be ± 0.05 eV. (k_x, k_y)-cuts at the Fermi surface cover approximately a *k*-space range ± 2 Å^{-1}.

STM was done at room temperature under UHV conditions ($p \approx 5 \times 10^{11}$ mbar) using an *Omicron VT–STM*.

X-ray absorption spectroscopy (XAS) was performed in the total electron yield (TEY) mode at the synchrotron *SOLARIS–XAS* beamline—using circularly polarized light at variable temperatures and magnetic fields up to 0.2 T.

Synchrotron-excited XPS was done at the materials science beamline at the Elettra synchrotron. With respect to the standard laboratory XPS it provided Bi and Se CL spectra with higher energy resolution (0.2 eV instead of 1 eV), surface sensitivity (information depth 5 Å instead of 20 Å) and overall intensity (photoionization cross sections higher by a factor of 20–100).

Fitting of core level spectra from XPS and UPS experiments was done in the program `KolXPD` [https://www.kolibrik.net/kolxpd]. The estimation of the relative concentrations between Bi 5d and Se 3d, in figure 3 is based on respective fitting of spin–orbit split Voigt doublet areas, which are normalized to calculated photoionization cross sections [45]. A Shirley background is assumed in all cases. For Fe 2p spectra, the leading edges are fitted by Doniach–Šunjić profiles. Two Voigt components were added at higher binding energies.

Density functional theory (DFT) calculations were done in the local spin-density approximation (LSDA) and are based on the full-potential linear augmented plane wave (FP–LAPW) method, as implemented in the band structure program ELK [http://elk.sourceforge.net/]. Spin–orbit coupling has been included in the calculations. The full Brillouin zone has been sampled by about 8000 *k*-points. As a structure, we assumed a tetragonal PbO-structure (P4/nmm) β-FeSe with lattice constants $a = 0.3765$ nm and $c = 0.5518$ nm. The chalcogen height above the Fe plane is defined by the internal parameter $z = 0.255$ [46].

Acknowledgments

We thank Professor Hidde Brongersma for valuable discussions. This work was supported by the Czech Science Foundation (Grant No. 19-13659S) and EU FET Open RIA Grant No. 766566. The research was partially supported by the Ministry of Education, Youth and Sports of the Czech Republic LQ1601 (CEITEC 2020). Part of the research was carried out using the CzechNanoLab Research Infrastructure supported by MEYS (LM2018110). Photoemission experiments were performed at the NanoESCA facilities supported by the Ministry of Education, Youth and Sports of the Czech Republic through project CZ.02.1.01/0.0/0.0/16_013/0001406. We acknowledge CERIC-ERIC support for synchrotron measurements at SOLARIS (project 20182048) and ELETTRA (project 20192095). Regarding the synchrotron experiments we particularly thank Dr. Marcin Zając for the support and important discussions.

ORCID iDs

K Carva https://orcid.org/0000-0002-2275-1986
J Honolka https://orcid.org/0000-0001-9822-1263

References

[1] Gariglio S, Gabay M, Mannhart J and Triscone J-M 2015 *Phys.* C **514** 189
[2] Tan S *et al* 2013 *Nat. Mater.* **12** 634
[3] Miyata Y, Nakayama K, Sugawara K, Sato T and Takahashi T 2015 *Nat. Mater.* **14** 775
[4] Bazhirov T and Cohen M L 2013 *J. Phys.: Condens. Matter.* **25** 105506
[5] Liu X, Zhao L, He S, He J, Liu D, Mou D, Shen B, Hu Y, Huang J and Zhou X J 2015 *J. Phys.: Condens. Matter.* **27** 183201
[6] Hasan M Z and Kane C L 2010 *Rev. Mod. Phys.* **82** 3045
[7] Qi X-L and Zhang S-C 2011 *Rev. Mod. Phys.* **83** 1057
[8] Cavallin A, Sevriuk V, Fischer K N, Manna S, Ouazi S, Ellguth M, Tusche C, Meyerheim H L, Sander D and Kirschner J 2016 *Surf. Sci.* **646** 72
[9] Eich A *et al* 2016 *Phys. Rev.* B **94** 125437
[10] Manna S, Kamlapure A, Cornils L, Hänke T, Hedegaard E M J, Bremholm M, Iversen B B, Hofmann P, Wiebe J and Wiesendanger R 2017 *Nat. Commun.* **8** 14074
[11] He Q L, Liu H, He M, Lai Y H, He H, Wang G, Law K T, Lortz R, Wang J and Sou I K 2014 *Nat. Commun.* **5** 4247
[12] Singh U R, White S C, Schmaus S, Tsurkan V, Loidl A, Deisenhofer J and Wahl P 2013 *Phys. Rev.* B **88** 155124
[13] Průša S *et al* 2015 *Langmuir* **31** 9628
[14] Brongersma H, Draxler M, de Ridder M and Bauer P 2007 *Surf. Sci. Rep.* **62** 63
[15] Vališka M *et al* 2016 *Appl. Phys. Lett.* **108** 262402
[16] He X, Zhou W, Wang Z Y, Zhang Y N, Shi J, Wu R Q and Yarmoff J A 2013 *Phys. Rev. Lett.* **110** 156101
[17] Gonçalves P H R, Chagas T, Nascimento V B, dos Reis D D, Parra C, Mazzoni M S C, Malachias N and Magalhães-Paniago R 2018 *J. Phys. Chem. Lett.* **9** 954
[18] Gibson Q D *et al* 2013 *Phys. Rev.* B **88** 081108
[19] Vondráček M *et al* 2016 *Phys. Rev.* B **94** 161114
[20] Naumkin A V, Kraut-Vass A, Gaarenstroom S W and Powell C J 2000 NIST X-ray Photoelectron Spectroscopy Database *NIST Standard Reference Database* **20** Version 4.1
[21] Kriegner D, Harcuba P, Veselý J, Lesnik A, Bauer G, Springholz G and Holý V 2017 *J. Appl. Crystallogr.* **50** 369
[22] Jin W and Osgood R M 2019 *Adv. Phys.* X **4** 1688187
[23] Srivastava N, Gao Q, Widom M, Feenstra R M, Nie S, McCarty K F and Vlassiouk I V 2013 *Phys. Rev.* B **87** 245414
[24] Sutter P, Sadowski J T and Sutter E 2009 *Phys. Rev.* B **80** 245411
[25] Speck F, Ostler M, Besendörfer S, Krone J, Wanke M and Seyller T 2017 *Ann. Phys., Lpz.* **529** 1700046
[26] Locatelli A, Knox K R, Cvetko D, Mente T O, Nio M A, Wang S, Yilmaz M B, Kim P, Osgood R M and Morgante A 2010 *ACS Nano* **4** 4879
[27] Bianchi M, Guan D, Bao S, Mi J, Iversen B B, King P D C and Hofmann P 2010 *Nat. Commun.* **1** 128
[28] Scholz M R, Sánchez-Barriga J, Marchenko D, Varykhalov A, Volykhov A, Yashina L V and Rader O 2012 *Phys. Rev. Lett.* **108** 256810
[29] Seah M P and Spencer S J 2002 *Surf. Interface Anal.* **33** 640
[30] Arnold F *et al* 2018 *J. Phys.: Condens. Matter.* **30** 065502
[31] Watson M D, Backes S, Haghighirad A A, Hoesch M, Kim T K, Coldea A I and Valentí R 2017 *Phys. Rev.* B **95** 081106
[32] Tan S Y *et al* 2016 *Phys. Rev.* B **93** 104513
[33] Bazhirov T and Cohen M L 2013 *J. Phys.: Condens. Matter.* **25** 105506
[34] Zheng F, Wang Z, Kang W and Zhang P 2013 *Sci. Rep.* **3** 2213
[35] Yokoya T *et al* 2012 *Sci. Technol. Adv. Mater.* **13** 054403
[36] Saini N L *et al* 2011 *Phys. Rev.* B **83** 052502
[37] Takubo K *et al* 2017 *Phys. Rev.* B **96** 115157
[38] Thole B T and van der Laan G 1988 *Phys. Rev.* B **38** 3158
[39] Honolka J *et al* 2009 *Phys. Rev.* B **79** 104430
[40] Sessi V *et al* 2014 *New J. Phys.* **16** 062001
[41] Crocombette J P, Pollak M, Jollet F, Thromat N and Gautier-Soyer M 1995 *Phys. Rev.* B **52** 3143
[42] Schlenk T *et al* 2013 *Phys. Rev. Lett.* **110** 126804
[43] Kim Y, Lee G, Li N, Seo J, Kim K S and Kim N 2019 *npj 2D Mater. Appl.* **3** 51
[44] Vondrácek M, Kalita D, Kucera M, Fekete L, Kopecek J, Lancok J, Coraux J, Bouchiat V and Honolka J 2016 *Sci. Rep.* **6** 23663
[45] Yeh J and Lindau I 1985 *At. Data Nucl. Data Tables* **32** 1
[46] Koufos A P, Papaconstantopoulos D A and Mehl M J 2014 *Phys. Rev.* B **89** 035150